Plasmonics
DOI 10.1007/s11468-017-0607-0

Multi-Band Plasmonic Platform Utilizing UT-Shaped Graphene Antenna Arrays

Yasa Ekşioğlu[1] · **Arif E. Cetin**[2] · **Habibe Durmaz**[3]

Received: 30 January 2017 / Accepted: 9 May 2017

Abstract In this work, we introduce a plasmonic platform based on UT-shaped graphene antenna arrays. The proposed multi-resonant platform shows three different resonances, which can be independently tuned. The physical origin of these modes is shown with finite-difference time-domain (FDTD) nearfield distribution analyses, which are used to statically tune each resonance wavelength via the geometrical parameters, corresponding to different nearfield localization. We achieve statistical tuning of multiple resonances also by changing the number of graphene layers. Another static tuning of the optical response of the UT-shaped graphene antenna is achieved via the chemical potential and the relaxation time.

Keywords Surface plasmon · Graphene plasmonics · Multi-band

Introduction

Surface plasmons (SPs) are the collective electron oscillations, propagating at an interface between a metal and a dielectric. The confinement of light through these surface waves with large nearfield intensity enhancements [1–3] enables various applications, i.e., surface-enhanced vibrational spectroscopy [4–6], label-free biosensing [7, 8] and high-efficiency photovoltaics [9]. Recently, graphene has been utilized in plasmonics due to its metallic behavior at mid- to far-IR spectral range such that it can control, confine, and manipulate light through SP excitation [10–13]. In that sense, collective oscillations of the electrons (or hole) gas in two-dimensional graphene sheets can produce guided electromagnetic waves with strong sub-wavelength confinement. Plasmonic resonances occur at mid-infrared and terahertz frequencies for typical carrier densities (several 10^{12} cm^{-2}) of graphene as opposed to visible or near-infrared excitations of traditional metallic plasmonic structures. As a result of these favorable properties, graphene plasmons covering mid- to far-IR frequency ranges have been extensively used in theoretical and experimental studies [13–24]. In addition, several device applications have been reported, including optoelectronic devices [14], ultrafast transistor-based photodetectors [25–27], optical modulators [28, 29], light emitters [30, 31], transparent solar cells [32], and biosensors [33, 34].

In this work, we introduce a plasmonic platform based on multi-resonant UT-shaped graphene plasmonic antenna arrays as shown in Fig. 1. The platform supports three distinct plasmonic resonances in the THz frequency range. The resonance frequencies depend on the geometrical device parameters, chemical potential, relaxation time, number of graphene layers, which are extensively investigated by finite-difference time-domain (FDTD) simulations. The paper is organized as follows: in "Methods" section, we explain the conductivity relation in graphene and express its plasmonic behavior in terms of conductivity. In "Results" section, we introduce the UT-shaped graphene antenna system on a thin SiN film. The effect of geometrical parameters on the spectral position of each plasmonic resonance is investigated in detail.

✉ Yasa Ekşioğlu
yasa.eksioglu@kemerburgaz.edu.tr

[1] Department of Electrical and Electronics Engineering, Istanbul Kemerburgaz University, Mahmutbey Dilmenler Caddesi, No: 26, 34217 Bağcılar, Istanbul, Turkey

[2] Koch Institute for Integrative Cancer Research, Massachusetts Institute of Technology, Cambridge, MA 02139, USA

[3] Department of Electrical and Electronics Engineering, Recep Tayyip Erdoğan University, Zihni Derin Yerleşkesi, Fener Mahallesi, 53100 Rize, Turkey

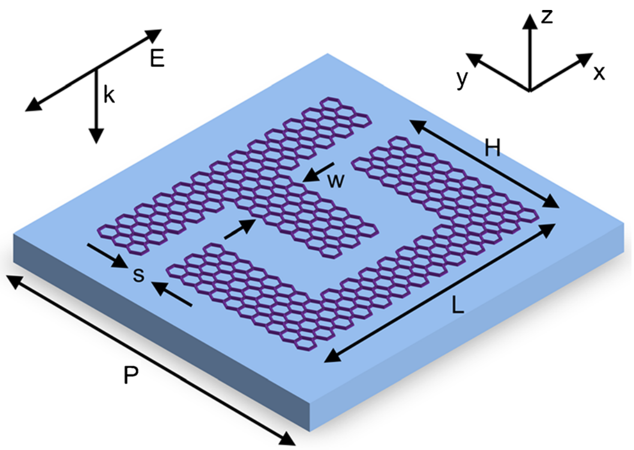

Fig. 1 Schematic view of the UT-shaped graphene antenna. The geometrical device parameters are *H* (height), *L* (length), *w* (rod width), *s* (distance between U- and T-antennas), and *P* is the period of the antenna array. The graphene structure stands on a SiN (silicon nitride) substrate (denoted with blue)

The physical origin of each plasmonic mode is shown in nearfield analyses with FDTD simulations. The effect of chemical potential, relaxation time, and the number of the graphene layers on the multi-band response is investigated. Such graphene geometry can be experimentally achieved by electron beam lithography (EBL)-based nano-fabrication techniques. In this paper, we theoretically investigate the multi-band behavior, and experimental characterization of the system will be demonstrated later. Commercial graphene grown by chemical vapor deposition (CVD) on copper foil can be used to have a large continuous sheet of graphene. First, poly(methyl methacrylate) (PMMA) is covered onto graphene on copper foil in order to prepare a supporting layer film. Then, the copper foil is etched away with copper etchant to have a free-standing graphene layer, which is floating on the surface of copper etchant. By using a SiN substrate, this floating sheet of graphene is fished out on top of the substrate with a following acetone bath to remove PMMA and a dry annealing process. After obtaining a large continuous sheet of graphene layer, EBL is implemented in order to pattern the UT-shaped antennas, which followed by plasma ashing to etch away the graphene outside of the UT-shape. Finally, the acetone bath and another annealing process are applied to clean out any undesired residue.

Methods

The linear response theory investigates the dynamic behavior of a condensed-matter system at thermal equilibrium in the presence of a small external field. The response of the system is expressed by Kubo formula [34–38]. If an external electric field is applied, the response of the system and the linear response coefficient are represented by current and conductivity, respectively. The optical response of graphene is determined by its conductivity where the relaxation time $\tau = \mu_c\mu/ev_F^2$, $\mu_c = \hbar v_f\sqrt{\pi n}$, $v_F = 10^6 m/s$, and μ_c is the chemical potential, e is the elementary charge, μ is the carrier mobility of the electrons in graphene which is less than the frequency applied ($\tau^{-1} \ll \hbar\omega$, ω is the frequency and $\hbar$ is the reduced Planck constant), and n is the carrier density [39]. From these relations, carrier density can be calculated as $n = (e^2 v_F^2 \tau^2)/(\pi \mu_c^2 \hbar^2)$. For a given chemical potential of $\mu_c = 0.4$ ***and*** $\tau = 0.5$ **ps**, the carrier density is $n = 1.47 \times 10^{13}$ cm^{-2}, where mobility of the graphene is chosen as 10000 cm^2/Vs from the [40]. According to graphene's semiconducting characteristics, conductivity of graphene that consists of inter- and intra-band transitions ($\sigma = \sigma_{intra} + \sigma_{inter}$) [38] is mainly controlled by the electron-hole excitations. The corresponding conductivity of graphene is written as:

$$\sigma(\omega) = \frac{e^2\omega}{i\pi\hbar}\left[\int_{-\infty}^{+\infty} d\varepsilon \frac{|\varepsilon|}{\omega^2}\frac{df_0(\varepsilon)}{d\varepsilon} - \int_0^{+\infty} d\varepsilon \frac{f_0(-\varepsilon) - f_0(\varepsilon)}{(\omega + i\delta)^2 - 4\varepsilon^2}\right] \quad (1)$$

where, T is finite temperature, $f_0(\varepsilon) = 1/\left(e^{(\varepsilon - \mu_c)}/T + 1\right)$ is the Fermi-Dirac distribution, and ε is the energy. Equation 1

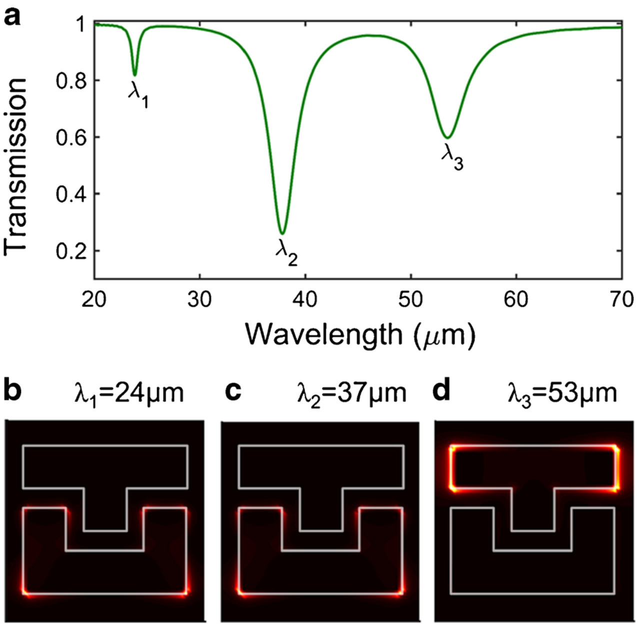

Fig. 2 **a** Transmission spectrum of UT-shaped graphene antenna arrays, where $\mu_c = 0.4$ ***eV***, $N = 1$, and $\tau = 0.5$ ***ps***. Corresponding device parameters are $H = 0.2$ ***μm***, $L = 0.4$ ***μm***, $s = 0.05$ ***μm***, $w = 0.1$ ***μm***, and $d = 0.07$ ***μm***. The total electric field intensities, $|\mathbf{E}|^2$, are shown for the three distinct transmission resonances at **b** $\lambda_1 = 24$ ***μm***, **c** $\lambda_2 = 37$ ***μm***, and **d** $\lambda_3 = 53$ ***μm***

Fig. 3 **a** Transmission spectrum of UT-shaped graphene antenna arrays with $H = 0.15\ \mu m$, $H = 0.2\ \mu m$, and $H = 0.25\ \mu m$, where $\mu_c = 0.4\ eV$, $N = 1$, $\tau = 0.5\ ps$, $L = 0.4\ \mu m$, $s = 0.05\ \mu m$, $w = 0.1\ \mu m$, and $d = 0.07\ \mu m$. **b** Spectral position vs. H for three distinct resonances at λ_1, λ_2, and λ_3

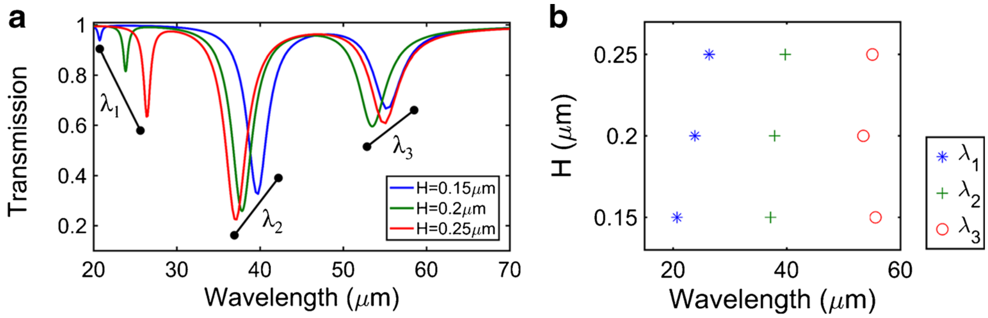

can be evaluated in the local limit of the random phase approximation (RPA) with finite $\boldsymbol{T}$ and finite relaxation time $\boldsymbol{\tau}$ [41–43].

$$\boldsymbol{\sigma}(\boldsymbol{\omega}) = \frac{2\boldsymbol{e}^2\boldsymbol{T}}{\pi\hbar}\frac{\boldsymbol{i}}{\boldsymbol{\omega}+\boldsymbol{i\tau}^{-1}}\log\left[2\cosh\left(\boldsymbol{\mu_c}/2\boldsymbol{k_B T}\right]\right. + \frac{\boldsymbol{e}^2}{4\hbar}\left[\boldsymbol{H}\left(\omega/2\right) + \frac{4\boldsymbol{i\omega}}{\pi}\int_0^\infty \boldsymbol{d\varepsilon}\frac{\boldsymbol{H}(\varepsilon)-\boldsymbol{H}\left(\omega/2\right)}{\omega^2-4\varepsilon^2}\right] \tag{2}$$

where $\boldsymbol{H}(\varepsilon) = \sinh(\hbar\varepsilon/\boldsymbol{k_B T})/(\cosh(\boldsymbol{\mu_c}/\boldsymbol{k_B T}) + \cosh(\hbar\varepsilon/\boldsymbol{k_B T}))$ and $\boldsymbol{k_B}$ is the Boltzmann constant. The first term in Eq. (2 is known as intra-band, and the second term corresponds to inter- and scattering process. At low frequencies, Drude response for intra-band transitions dominates when $1/\boldsymbol{\tau} = 0$ [35].

$$\boldsymbol{\sigma}(\boldsymbol{\omega})_{\text{intra}} = \boldsymbol{i}\frac{2\boldsymbol{e}^2\boldsymbol{T}}{\pi\hbar\boldsymbol{\omega}}\log\left[2\cosh\left(\boldsymbol{\mu_c}/2\boldsymbol{k_B T}\right]\right. \tag{3}$$

At high frequencies, inter-band transitions dominate with $\boldsymbol{\delta} = 0$ and in terms of step function.

$$\boldsymbol{H}\left(\omega/2\right) = \boldsymbol{\theta}(\omega-2\boldsymbol{\mu_c})\ \text{for}\ \boldsymbol{\mu_c} \gg \boldsymbol{k_B T}.$$

$$\boldsymbol{\sigma}(\boldsymbol{\omega})_{\text{inter}} = \frac{\boldsymbol{e}^2}{4\hbar}\left[\boldsymbol{\theta}(\hbar\boldsymbol{\omega}-2\boldsymbol{\mu_c})-\frac{\boldsymbol{i}}{\pi}\log\left|\frac{\hbar\boldsymbol{\omega}-2\boldsymbol{\mu_c}}{\hbar\boldsymbol{\omega}+2\boldsymbol{\mu_c}}\right|\right] \tag{4}$$

Inter-band transitions occur when $\hbar\boldsymbol{\omega} \geq 2\boldsymbol{\mu_c}$ at short wavelengths. In order to analyze graphene plasmons, intra-band transitions are considered, $\hbar\boldsymbol{\omega} < 2\boldsymbol{\mu_c}$, in mid- and far-IR frequency ranges. The dispersion relation for surface plasmons can be derived from Dyadic Green's functions for a surface model of graphene by considering incoming TE and TM plane waves under boundary conditions [36]. In the presence of high doping, TM mode (related with intra-band transitions of conductivity) dominates such that the dispersion relation is described by $\boldsymbol{k_{SP}} \approx \boldsymbol{i\omega}(\epsilon + 1)/4\boldsymbol{\pi\sigma}$ [43].

The Drude formula is inserted to the surface plasmon dispersion relation, which yields $\boldsymbol{k_{SP}} \approx (\hbar^2/4\boldsymbol{e}^2\boldsymbol{\mu_c})(\epsilon + 1)\boldsymbol{\omega}(\boldsymbol{\omega} + \boldsymbol{i\tau}^{-1})$, i.e., the corresponding resonance wavelength is ($\boldsymbol{\lambda_{SP}}/\boldsymbol{\lambda}_0) \approx (\boldsymbol{\mu_c}/\hbar\boldsymbol{\omega})(4\boldsymbol{\alpha}/(\epsilon + 1))$, where $\boldsymbol{\alpha} = (1/4\boldsymbol{\pi}\epsilon_0)(\boldsymbol{e}^2/\hbar\boldsymbol{c})$ is the fine structure constant, ϵ_0 is the permittivity of the free space, and $\boldsymbol{c}$ is the speed of light in vacuum.

Results

We investigate the dependence of the optical behavior of UT-shaped graphene antennas on geometrical and other material parameters by FDTD simulations (Lumerical Solutions Inc.) [44]. The antenna system supports multi-band spectral response similarly to its plasmonic nanoparticle meta-material analog [45]. The geometrical parameters play an important role in the spectral position of the plasmonic resonances (observed as transmission minima) and provide a fine-tuning mechanism of spectral responses. The schematics of UT-shaped graphene are presented in Fig. 1, where the geometrical device parameters are H (height), L (length), w (rod width), s (distance between U- and T- antennas), and P is the period of

Fig. 4 **a** Transmission spectrum of UT-shaped graphene antenna arrays with $L = 0.35\ \mu m$, $L = 0.4\ \mu m$, and $L = 0.45\ \mu m$, where $\mu_c = 0.4\ eV$, $N = 1$, $\tau = 0.5\ ps$, $H = 0.2\ \mu m$, $s = 0.05\ \mu m$, $w = 0.1\ \mu m$, and $d = 0.07\ \mu m$. **b** Spectral position vs. L for three distinct resonances at λ_1, λ_2, and λ_3

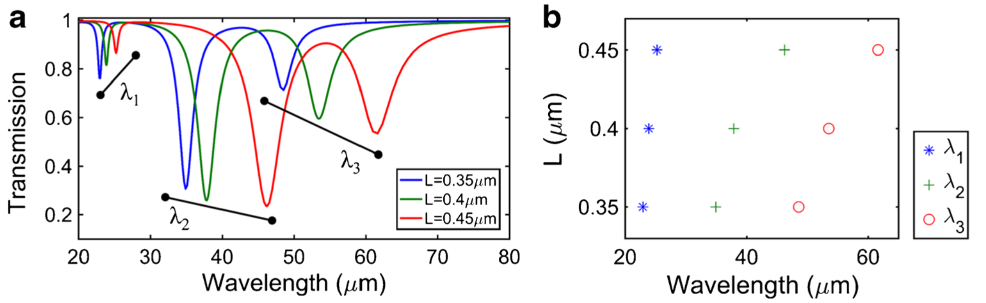

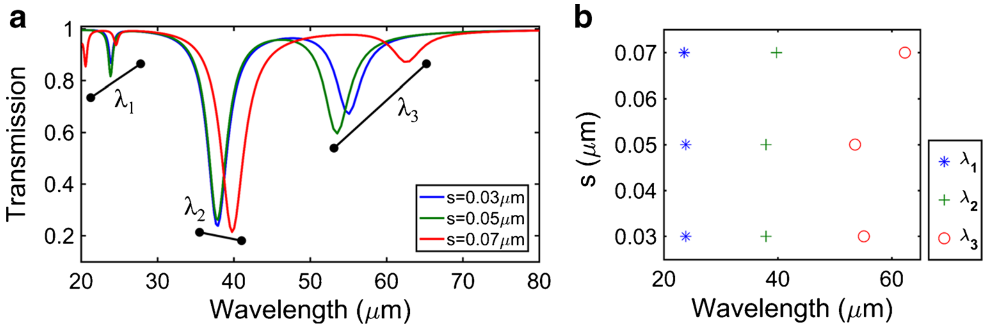

Fig. 5 **a** Transmission spectrum of UT-shaped graphene antenna arrays with $s = 0.03\ \mu m$, $s = 0.05\ \mu m$, and $s = 0.07\ \mu m$, where $\mu_c = 0.4\ eV$, $N = 1$, $\tau = 0.5\ ps$, $H = 0.2\ \mu m$, $L = 0.4\ \mu m$, $w = 0.1\ \mu m$, and $d = 0.07\ \mu m$. **b** Spectral position vs. s for three distinct resonances at λ_1, λ_2, and λ_3

the antenna array. The graphene structure stands on a (silicon nitride) SiN substrate. Normally, incident light source impinges on the graphene substrate, polarized along the long edge of the antennas as depicted in the figure. In our numerical analyses, the intra-band conductivity of graphene at low frequencies is modeled with Drude approximation at $T = 300\ K$ and scattering length $\Gamma = 1/2\tau$, where the total conductivity is studied at the entire far-IR frequency range.

Along $\boldsymbol{x}$- and $\boldsymbol{y}$-axes, periodic boundary condition is used and along the direction of the incident light (z), perfectly matched layer is used. As shown in Fig. 2a, the graphene antenna arrays supports three distinct transmission resonances at $\boldsymbol{\lambda}_1 = 24\ \boldsymbol{\mu m}$, $\boldsymbol{\lambda}_2 = 37\ \boldsymbol{\mu m}$, and $\boldsymbol{\lambda}_3 = 53\ \boldsymbol{\mu m}$. In Fig. 2b, d, total electric field intensities ($|\boldsymbol{E}|^2$) at air-graphene interface are presented for the resonances. The first (at $\boldsymbol{\lambda}_1$) and second (at $\boldsymbol{\lambda}_2$) modes are originated from the constituting U-shaped graphene antenna, while the third one (at $\boldsymbol{\lambda}_3$) is associated with the T-shaped structure. The electromagnetic field intensity enhancement calculated on the top surface of the graphene is due to the excitation of localized surface plasmons, which show a dipolar character and induces strong nearfield enhancements particularly on the edge of the constituting U- and T-shaped antennas.

First, we investigate the dependence of the transmission spectrum of the UT-shaped graphene antenna on the geometrical device parameters. In Fig. 3a, $\boldsymbol{H}$ (height) is varied, while the other parameters are kept constant. The mode at $\lambda_1 = 24\ \mu m$ shifts to longer wavelengths, while the one at $\lambda_2 = 37\ \mu m$ shifts to shorter wavelengths with H (Fig. 3b).

This is due to the fact that, for these modes, the local electromagnetic fields concentrate along the arms of the constituting U-shaped antenna, i.e., varying $\boldsymbol{H}$ strongly affects the position of these modes. On the other hand, the mode at $\boldsymbol{\lambda}_3 = 53\ \boldsymbol{\mu m}$ shows unpredictable spectral variations as the local electromagnetic fields associated with this mode concentrate at antenna elements which are not characterized by $\boldsymbol{H}$ variations, i.e., we observe blue and red shifts for $\boldsymbol{H} = 0.3\ \boldsymbol{\mu m}$ and $\boldsymbol{H} = 0.25\ \boldsymbol{\mu m}$, respectively.

In Fig. 4a, we show the dependence of the transmission resonances on $\boldsymbol{L}$ (length). Analog to Fabry-Perot resonator for nano-antenna configurations, dipolar resonances appear at integer multiples of resonant wavelength which is linearly proportional to the length, along the polarization direction [46–48]. Similarly for the UT-shaped graphene antenna, the increase in the length shifts the resonances wavelength of all three modes to longer wavelengths as $\boldsymbol{L}$ variation alters the lengths of rod which

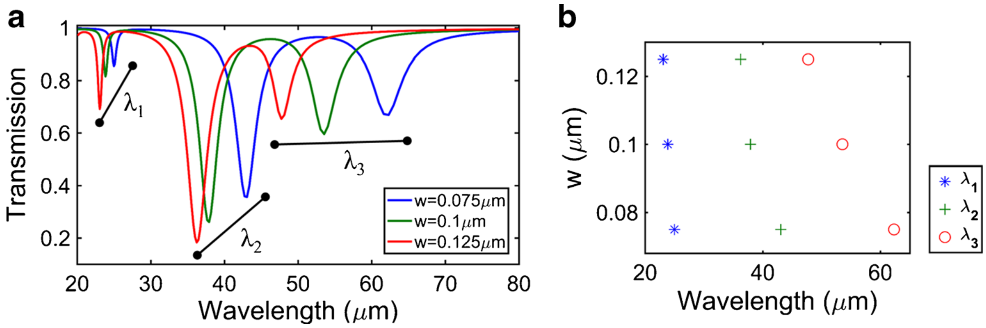

Fig. 6 **a** Transmission spectrum of UT-shaped graphene antenna arrays with $w = 0.075\ \mu m$, $w = 0.1\ \mu m$, and $w = 0.125\ \mu m$, where $\mu_c = 0.4\ eV$, $N = 1$, $\tau = 0.5\ ps$, $H = 0.2\ \mu m$, $L = 0.4\ \mu m$, $s = 0.05\ \mu m$, and$d = 0.07\ \mu m$. **b** Spectral position vs. w for three distinct resonances at λ_1, λ_2, and λ_3

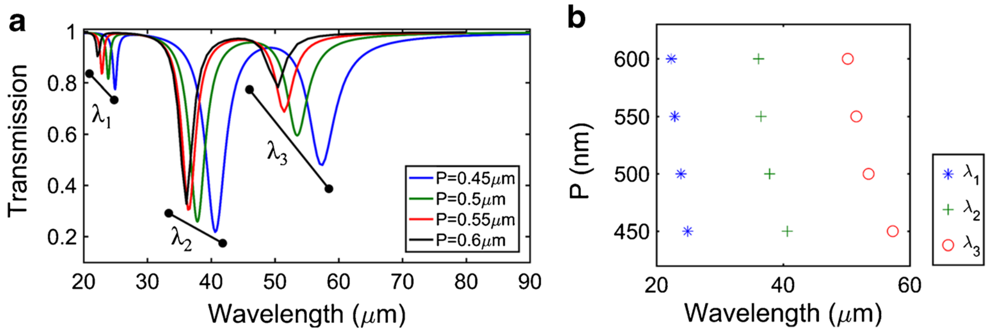

Fig. 7 **a** Transmission spectrum of UT-shaped graphene antenna arrays with $P = 0.45\ \mu m$, $P = 0.5\ \mu m$, $P = 0.55\ \mu m$, and $P = 0.6\ \mu m$, where $\mu_c = 0.4\ eV$, $N = 1$, $\tau = 0.5\ ps$, $H = 0.2\ \mu m$, $L = 0.4\ \mu m$, $w = 0.1\ \mu m$ $s = 0.05\ \mu m$, and $d = 0.07\ \mu m$. **b** Spectral position vs. P for three distinct resonances at λ_1, λ_2, and λ_3

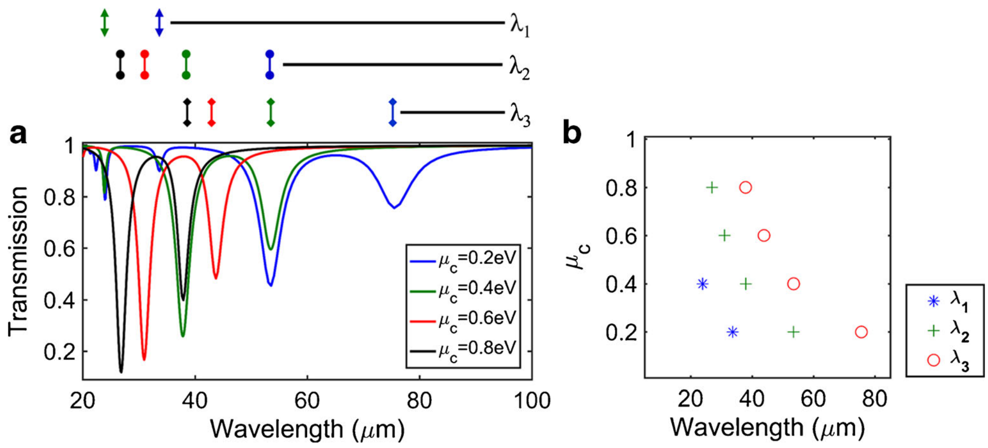

Fig. 8 **a** Transmission spectrum of UT-shaped graphene antenna arrays with $\mu_c = 0.2\ eV$, $\mu_c = 0.4\ eV$, $\mu_c = 0.6\ eV$, and $\mu_c = 0.8\ eV$, where $N = 1$, $\tau = 0.5\ ps$, $H = 0.2\ \mu m$, $L = 0.4\ \mu m$, $P = 0.5\ \mu m$, $w = 0.1\ \mu m$ $s = 0.05\ \mu m$, and $d = 0.07\ \mu m$. **b** Spectral position vs. μ_c for three distinct resonances at λ_1, λ_2, and λ_3. For a constant $\tau = 0.5\ ps$, the carrier densities are 7.35×10^{12}, 1.47×10^{13}, 2.2×10^{13}, and $3 \times 10^{13}\ \text{cm}^{-2}$ for $\mu_c = 0.2$, 0.4 , 0.6 , *and* $0.8\ eV$, respectively

belong to the constituting U- and T-shaped antennas along the polarization direction (Fig. 4a). Figure 4b, showing the spectral position of each transmission resonance for different ***L*** values, clearly demonstrates this linear relation. More importantly, the field localization at the edge of the rods for the mode at $\boldsymbol{\lambda}_3$ is stronger than those of the modes at $\boldsymbol{\lambda}_1$ and $\boldsymbol{\lambda}_2$ such that the shift in the transmission resonance corresponding this mode is larger compared to the later ones.

In Fig. 5, we investigate the effect of the distance between constituting U- and T-shaped graphene antennas (***s***) on the transmission resonances supported by the UT-shaped antenna. We observe that the spectral position of the mode at $\boldsymbol{\lambda}_1$ remains unchanged for different values of $\boldsymbol{s} = 0.03\boldsymbol{\mu m}$, $0.05\boldsymbol{\mu m}$, and $0.07\boldsymbol{\mu m}$, while its amplitude varies. On the other hand, the one at $\boldsymbol{\lambda}_2$ experiences a slight red-shift, while its amplitude does not vary. Unlike the other modes, the mode at $\boldsymbol{\lambda}_3$ shows both blue and red shifts for different ***s*** values, suggesting a critical distance between the constituting antennas in the composite structure, which plays the dominant role for the interference between these elements. Here, the mode at $\boldsymbol{\lambda}_3$ experiences a large spectral shift compared to the others, as the field localization for this mode is much stronger at the antenna edges of the constituting T-shaped antenna, where ***s*** variation mainly alters.

In Fig. 6a, we investigate the dependence of the transmission resonances supported by the UT-shaped graphene antenna array on the width of the antenna (***w***). All three resonant modes show similar spectral behavior for larger width, i.e.,

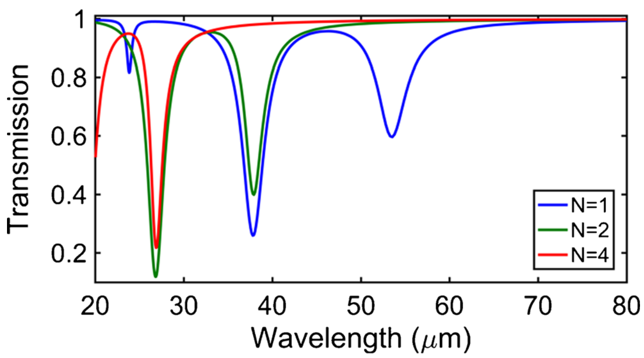

Fig. 9 Transmission spectrum of UT-shaped graphene antenna arrays with $N = 1$, $N = 2$, and $N = 4$, where $\mu_c = 0.4\ eV$, $\tau = 0.5\ ps$, $H = 0.2\ \mu m$, $L = 0.4\ \mu m$, $P = 0.5\ \mu m$, $w = 0.1\ \mu m$, $s = 0.05\ \mu m$, and $d = 0.07\ \mu m$

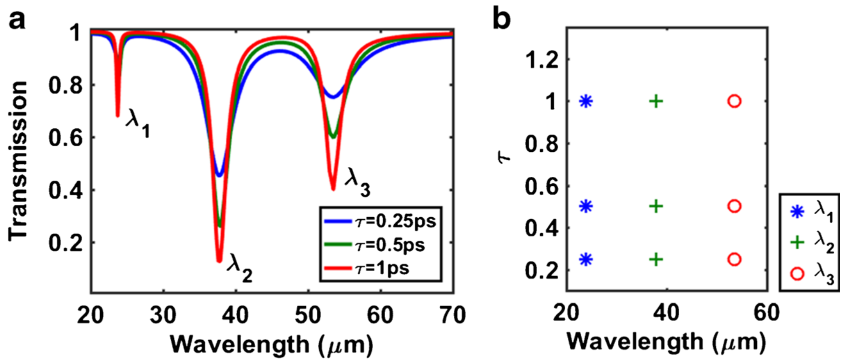

Fig. 10 **a** Transmission spectrum of UT-shaped graphene antenna arrays with $\tau = 0.25\ ps$, $\tau = 0.5\ ps$, and $\tau = 1\ ps$, where $\mu_c = 0.4\ eV$, $N = 1$, $H = 0.2\ \mu m$, $L = 0.4\ \mu m$, $P = 0.5\ \mu m$, $w = 0.1\ \mu m$, $s = 0.05\ \mu m$, and $d = 0.07\ \mu m$. **b** Spectral position vs. τ for three distinct resonances at λ_1, λ_2, and λ_3. For a given chemical potential of $\mu_c = 0.4$ *and* $\tau = 0.25$, 05 , and 1ps, the carrier densities are 7.35 × 10^{12}, 1.47 × 10^{13}, and 3 × 10^{13} cm^{-2}, respectively

they shift to shorter wavelengths and their transmission amplitude increases.

In Fig. 7, at all three resonant modes at $\boldsymbol{\lambda}_1 = 24\ \boldsymbol{\mu m}$, $\boldsymbol{\lambda}_2 = 37\ \boldsymbol{\mu m}$,and $\boldsymbol{\lambda}_3 = 53\boldsymbol{\mu m}$, for larger periods, transmission resonances shifts to shorter wavelengths. This is due to the decrease in the coupling between each UT-shaped antenna in the array, as the separation between them increases [6]. We also observe a reduction in the transmission for larger periodicity. One reason behind this again is the weakening of the coupling strength between each UT-shaped antenna. The second reason is that as the period increases, the ratio between the number of photon impinges on the UT-shaped antenna and that of the incident photon increases.

The chemical potential, $\boldsymbol{\mu_c}$, for electrons refers to a Fermi level ($\mu_c \approx \boldsymbol{E_F} \approx \hbar v_f k_f$, where $\boldsymbol{k_f}$ is the diameter of Fermi sphere), and Drude model at low frequencies is $\boldsymbol{\sigma}(\boldsymbol{\omega}) = (\boldsymbol{e}^2\boldsymbol{\mu_c}/\pi\hbar^2)(\boldsymbol{i}/\boldsymbol{\omega} + \boldsymbol{i}\boldsymbol{\tau}^{-1})$ with $\boldsymbol{\mu_c} \gg \boldsymbol{k_B T}$. From the definition of the Drude model, larger μ_c induces an increase in the conductivity. Inserting $\boldsymbol{\sigma}(\boldsymbol{\omega})$ to the definition of the plasmonic wavelength, $\boldsymbol{\lambda_{sp}} = 2\eta\omega \boldsymbol{Re}[\boldsymbol{k_{sp}}/\boldsymbol{k}_0]$, we can obtain the resonant wavelength as a function of Fermi energy [49–51]:

$$\lambda_{sp} = \frac{2\pi\hbar c}{e}\sqrt{\frac{\eta\varepsilon_0(\varepsilon_{r1} + \varepsilon_{r2})\omega}{E_F}} \tag{5}$$

where $\boldsymbol{\eta}$ is dimensionless constant (function of $\boldsymbol{E_F}$), which represents the electrodynamic response of the graphene plasmonic structure. Knowing the fact stated above $\mu_c \approx \boldsymbol{E_F}$ transmission resonances shift toward shorter wavelength (Fig. 8). Furthermore, as plasmonic oscillations increase with the number of carriers, transmission corresponding to these resonances increases.

In Fig. 9, we investigate the effect of the number of graphene layer ($\boldsymbol{N}$) on the transmission spectra of the antenna system. The total optical conductivity can be evaluated by considering the individual layers as $\boldsymbol{N\sigma_T}(\boldsymbol{\omega})$ [52], where $\boldsymbol{\sigma_T}(\boldsymbol{\omega})$ is the total dynamical conductivity. For larger number of layers, number of electrons that contributes to the plasmonic oscillations increases. Thus, the corresponding transmission spectra shifts to shorter wavelengths from $\boldsymbol{N} = 1$ to $\boldsymbol{N} = 4$. After $\boldsymbol{N} = 4$, for the spectral window of interest, multi-band behavior is no longer observed.

The carrier mobility and chemical potential are strongly related to the relaxation time of electrons in graphene, e.g., $\boldsymbol{\tau} = \boldsymbol{\mu_c}\ \boldsymbol{\mu}/\boldsymbol{e}\boldsymbol{v_f}^2$, where $\boldsymbol{\mu}$ can be tuned by changing carrier concentration through doping with another molecule. In Fig. 10a, transmission spectrum of the UT-shaped graphene antenna array is presented for different $\boldsymbol{\tau}$ values, while other parameters are kept constant. The resonance peak remains constant with $\boldsymbol{\tau}$ for all transmission resonances. On the other hand, the amplitude of the transmission peak increases with larger number of carriers that contributes to the plasmonic oscillations.

Conclusion

In conclusion, we introduce a multi-band UT-shaped graphene antenna arrays. The antenna platform supports three resonances, where their peak wavelength depends on the geometry of the structure, suggesting a fine-tuning mechanism of optical responses. The physical origin of this dependence is investigated by nearfield calculations. We also investigate the effect of chemical potential, number of graphene layers, and relaxation time on the transmission spectrum of the UT-shaped graphene antenna.

Acknowledgements Yasa Ekşioğlu acknowledges the support of Istanbul Kemerburgaz University Scientific Research Foundation project No: PB2016-I-012.

References

1. Stern EA, Ferrell RA (1960) Surface plasma oscillations of a degenerate electron gas. Phys Rev 120:130–136
2. Ozbay E (2006) Plasmonics: merging photonics and electronics at nanoscale dimensions. Science 311:189–193
3. Maier SA (2007) Plasmonics: fundamentals and applications. Springer, New York
4. Kneipp K, Wang Y, Kneipp H, Perelman LT, Itzkan I, Dasari RR, Field MS (1997) Single molecule detection using surface-enhanced Raman scattering (SERS). Phys Rev Lett 78:1667–1670
5. Kundu J, Le F, Nordlander P, Halas NJ (2008) Surface enhanced infrared absorption (SEIRA) spectroscopy on nanoshell aggregate substrates. Chem Phys Lett 452:115–119
6. Adato R, Yanik AA, Amsden JJ, Kaplan DL, Omenetto FG, Hong MK, Erramili S, Altug H (2009) Ultra-sensitive vibrational spectroscopy of proteinmonolayers with plasmonic nanoantenna arrays. Proc Natl Acad Sci U S A 106:19227–19232
7. Kabashin AV, Evans P, Pastkovsky S, Hendren W, Wurtz GA, Atkinson R, Pollard R, Podolskiy VA, Zayats AV (2009) Plasmonic nanorod metamaterials for biosensing. Nat Mater 8: 867–871
8. Artar A, Yanik AA, Altug H (2009) Fabry–Pérot nanocavities in multilayered plasmonic crystals for enhanced biosensing. Appl Phys Lett 95:051105
9. Atwater HA, Polman A (2010) Plasmonics for improved photovoltaic devices. Nat Mater 9:205–213
10. Grigorenko AN, Polini M, Novoselov KS (2012) Graphene plasmonics. Nat Photonics 6:749–758
11. Low T, Avouris P (2014) Graphene plasmonics for terahertz to mid-infrared applications. ACS Nano 8:1086–1101
12. Garcia de Abajo FJ (2014) Graphene plasmonics: challenges and opportunities. ACS Photon 1:35–152
13. Geim AK, Novoselov KS (2007) The rise of graphene. Nat Mater 6: 183–191
14. Bonaccorso F, Sun Z, Hasan T, Ferrari AC (2010) Graphene photonics and optoelectronics. Nat Photonics 4:611–622
15. Song J, Zhang L, Xue Y, Yang Q, Wu S, Xia F, Zhang C, Zhong YL, Zhang Y, Teng J, Premaratne M, Qiu CW, Bao Q (2016) Efficient excitation of multiple plasmonic modes on three-dimensional graphene: an unexplored dimension. ACS Photonics 3:1986–1992
16. Liu PQ, Valmorra F, Maissen C, Faist J (2015) Electrically tunable graphene anti-dot array terahertz plasmonic crystals exhibiting multi-band resonances. Optica 2:135–140
17. Jablan M, Buljan H, Soljačić M (2009) Plasmonics in graphene at infrared frequencies. Phys Rev B 80:245435
18. Gao W, Shi G, Jin Z, Shu J, Zhang Q, Vajtai R, Ajayan PM, Kono J, Xu Q (2013) Excitation and active control of propagating surface plasmon polaritons in graphene. Nano Lett 13:3698–3702
19. Yan H, Low T, Zhu W, Wu Y, Freitag M, Li X, Guinea F, Avouris P, Xia F (2013) Damping pathways of mid-infrared plasmons in graphene nanostructures. Nat Photonics 7:394–399
20. Gao W, Shu J, Qiu C, Xu Q (2012) Excitation of plasmonic waves in graphene by guided-mode resonances. ACS Nano 6:7806–7813
21. Nene P, Strait J, Chan WM, Manolatou C, Kevek JW, Tiwari S, McEuen PL, Rana F (2013) Graphene micro- and nano-plasmonics. QTh1B.2 CLEO:2013 OSA
22. Li HJ, Zhai X, Sun B, Huang ZR, Wang LL (2015) A graphene-based bandwidth-tunable mid-infrared ultra-broadband plasmonic filter. Plasmonics 10:765–771
23. Said FA, Menon PS, Nawi MN, Md Zain AR, Jalar A, Majlis BY (2016) Copper-graphene SPR-based biosensor for urea detection. IEEE-ICSE Proc. doi:10.1109/SMELEC.2016.7573642
24. Lee JK, Kim H (2016) Mid-infrared plasmonic tuning via nanogap control in periodic multilayer graphene nanoribbons. Opt Mater 54: 22–25
25. Xia F, Mueller T, Lin YM, Valdes-Garcia A, Avouris P (2009) Ultrafast graphene photodetector. Nature NanoTech 4:839–843
26. Freitag M, Low T, Zhu W, Yan H, Xia F, Avouris P (2013) Photocurrent in graphene harnessed by tunable intrinsic plasmons. Nat Commun 4:1951
27. Cai X, Sushkov AB, Jadidi MM, Nyakiti LO, Myers-Ward RL, Gaskill DK, Murphy TE, Fuhrer MS, Drew HD (2015) Plasmon-enhanced terahertz photodetection in graphene. Nano Lett 15: 4295–4302
28. Ju L, Geng B, Horng J, Girit C, Martin M, Hao Z, Bechtel HA, Liang X, Zettl A, Shen YR, Wang F (2011) Graphene plasmonics for tunable terahertz metamaterials. Nat Nanotechnol 6:630–634
29. Sensale-Rodriguez B, Yan R, Zhu M, Jena D, Liu L, Xing HG (2012) Efficient terahertz electro-absorption modulation employing graphene plasmonic structures. Appl Phys Lett 101:261115
30. Otsuji T, Popov V, Ryzhii V (2014) Active graphene plasmonics for terahertz device applications. J Phys D Appl Phys 47:094006
31. Brar VW, Sherrott MC, Jang MS, Kim S, Kim L, Choi M, Sweatlock LA, Atwater HA (2015) Electronic modulation of infrared radiation in graphene plasmonic resonators. Nat Commun 6: 7032
32. Wang X, Zhi L, Mullen K (2008) Transparent, conductive graphene electrodes for dye-sensitized solar cells. Nano Lett 8:323–327
33. Rodrigo D, Limaj O, Janner D, Etezadi D, García de Abajo FJ, Pruneri V, Altug H (2015) Mid-infrared plasmonic biosensing with graphene. Sci Rep 349:165–168
34. Zhao Y, Hu X, Guanxiong C, Xuanru Z, Ziqi T, Junhua C, Rodney SR, Yanwu Z, Yalin L (2013) Infrared biosensors based on graphene plasmonics: modeling. Physical Chemistry Chem Phys 15:17118–17125
35. Falkovsky L, Pershoguba S (2007) Optical far-infrared properties of a graphene monolayer and multilayer. Phys Rev B 76:1–4
36. Hanson GW (2008) Dyadic Green's functions for an anisotropic, nonlocal model of biased graphene. IEEE Trans Antennas Propag 56:747–757
37. Falkovsky LA (2008) Optical properties of graphene. J Phys Conf Ser 129:012004
38. Gan CH, Chu HS, Li EP (2012) Synthesis of highly confined surface plasmon modes with doped graphene sheets in the mid infrared and terahertz frequencies. Phys Rev B 85:125431
39. Ke S, Wang B, Huang H, Long H, Wang K, Lu P (2015) Plasmonic absorption enhancement in periodic cross-shaped graphene arrays. Opt Express 23:8888–8900
40. Jablan M, Buljan H, Soljačić M (2009) Plasmonics in graphene at infrared frequencies. Phys Rev B 80:245435
41. Wunsch B, Stauber T, Sols F, Guinea F (2006) Dynamical polarization of graphene at finite doping. New J Phys 8:318
42. Hwang EH, S DS (2007) Dielectric function, screening, and plasmons in two-dimensional graphene. Phys Rev B 75: 205418
43. Koppens FH, Chang DE, de Abajo FJG (2011) Graphene plasmonics: a platform for strong light matter interactions. Nano Lett 11:3370–3377
44. Finite-difference-time-domain package, Lumerical FDTD Solutions (2014) [Online]. Available: www.lumerical.com
45. Cetin AE, Turkmen M, Aksu S, Altug H (2012) Nanoparticle-based metamaterials as multiband Plasmonic resonator antennas. IEEE Trans Nano Technol 11:208–212
46. Novotny L (2007) Effective wavelength scaling for optical antennas. Phys Rev Lett 98:266802
47. Liberman V, Adato R, Jeys TH, Saar BG, Erramilli S, Altug H (2012) Rational design and optimization of plasmonic nanoarrays for surface enhanced infrared spectroscopy. Opt Express 20:11953–11967

48. Cubukcu E, Capasso F (2009) Optical nanorod antennas as dispersive one-dimensional Fabry–Pérot resonators for surface plasmons. Appl Phys Lett 95:201101
49. Krasavin AV, Zayats AV (2008) Three-dimensional numerical modeling of photonic integration with dielectric-loaded SPP waveguides. Phys Rev B 78:045425
50. Holmgaard T, Bozhevolnyi SI (2007) Theoretical analysis of dielectric-loaded surface plasmon-polariton waveguides. Phys Rev B 75:245405
51. Wu L, Chu HS, Koh WS, Li EP (2010) Highly sensitive graphene biosensors based on surface plasmon resonance. Opt Express 18: 14395–14400
52. Chu HS, Choon HG (2013) Active plasmonic switching at mid-infrared wavelengths with graphene ribbon arrays. Appl Phys Lett 102:231107